Adhesion-mediated heterogeneous actin organization governs apoptotic cell extrusion

Anh Phuong Le[1,2], Jean-François Rupprecht[1], René-Marc Mège[3], Yusuke Toyama[1,5], Chwee Teck Lim[1,2,4,*], Benoît Ladoux[3,*]

[1]Mechanobiology Institute, National University of Singapore, Singapore

[2]National University of Singapore Graduate School of Integrative Sciences and Engineering, National University of Singapore, Singapore

[3]Université de Paris, CRS, Institut Jacques Monod (IJM), Paris, France

[4]Department of Biomedical Engineering, National University of Singapore, Singapore

[5]Department of Biological Sciences, National University of Singapore, Singapore

* Corresponding authors

Chwee Teck Lim
Email: ctlim@nus.edu.sg

Benoît Ladoux
Email: benoit.ladoux@ijm.fr

ABSTRACT

Apoptotic extrusion is crucial in maintaining epithelial homeostasis and has implications in diseases of epithelial tissues. Current literature supports that epithelia respond to extrusion to maintain their integrity by the formation of a supracellular actomyosin ring (purse-string) in the neighbors that encompasses the dying cells. However, little is known about whether other types of actin structures could contribute to extrusion as well as how forces generated by mechanosensitive proteins in the cells are integrated. Here, we found that during extrusion, a heterogeneous actin network composed of lamellipodia protrusions and discontinuous actomyosin cables, was reorganized in the neighboring cells and was the main factor driving extrusion forwards. The early presence of basal lamellipodia protrusion participated both in basal sealing of the extrusion site and in orienting the actomyosin purse-string at the later stage of extrusion. These sequential events are essential in ensuring a successful extrusion in apicobasal direction. The co-existence of these two mechanisms is determined by the interplay between the cell-cell and cell-substrate adhesions. A theoretical model integrates the role of these cellular mechanosensitive components to explain why a dual-mode mechanism, which combined lamellipodia protrusion and purse-string contractility, leads to more efficient extrusion than a single-mode mechanism. We anticipate that our approach will be useful to provide mechanistic insight into epithelial homeostasis, morphogenetic events and tumorigenesis.

INTRODUCTION

In adult homeostatic tissues, the epithelia undergo constant turnover with cell division balanced by cell death [1]. Maintaining integrity requires the removal of dead cells by extrusion to protect the organ they encase. To achieve this goal, rearrangement of neighboring cells occurs concurrently with apoptotic cell death to expel the dying cell while maintaining intact monolayer [2].

The purse-string model has been described as the primary extrusion mechanism in epithelia monolayers. During this process, contractile actomyosin rings are formed by the extruding cell itself [3, 4] and by the neighboring cells [4-6]. Both intrinsic and extrinsic apoptotic pathways can elicit extrusion, and caspase activation is essential to activate the Rho signaling pathway [7], which promotes the actomyosin ring formation in both the extruding cell and the neighboring cells. In mammalian cells, these rings were suggested to contract basolaterally and exert an upward force to expel the dying cell and close the gap left behind [4, 5]. There are similarities drawn between the actomyosin contractile ring here and the supracellular purse-string in the wound healing mechanism [8-10]. Nevertheless, cell extrusion involves three-dimensional cell-cell junction reorganization at the interface of dying cell-neighboring interface [11-13], while contractile purse-string in wound healing cases was described to exert forces in a single plane. Cells adjacent to the extrusion site partially lose polarity and reorganize their cell-cell junctions and actomyosin network [11, 14]. Thus, the presence of the extruding cell instead of a void gap, which involves the additional roles of cell-cell junctions at the interface between dying cells and neighboring cells, distinguishes extrusion from wound healing. Therefore, how actomyosin purse-string could produce sufficient force to drive extrusion in three-dimensionally in the polarized epithelia is still ambiguous.

Recently, we provided evidence that extrusion of apoptotic cells in epithelia with low packing density could occur with little purse-string involvement [15]. In this case, neighboring cells crawl towards extruding site and expel the dying cell via lamellipodia protrusions based on Rac1-regulated actin polymerization. This result is reminiscent of the wound healing process when heterogeneous actomyosin networks could concurrently contribute to gap closure with distinct force signature [16, 17]. Nevertheless, whether the presence of lamellipodia impedes purse-string formation during extrusion was not clarified in previous studies. Also, as cells extend lamellipodia, cell-extracellular matrix (ECM) interactions through focal adhesions

32 are remodeled, whether such dynamics of cell-substrate adhesions modulates actin

33 reorganization during extrusion has not been understood so far.

34   In this study, we sought to determine the relative contributions of cell crawling and cell

35 contractility to extrusion in relation with cell-cell and cell substrate adhesions. We addressed

36 these questions using MDCK cell culture as the model and a combination of techniques

37 including laser-induced cell death, micro-patterning, traction force microscopy, and molecular

38 biology.

39

40 **RESULTS**

41 **Extrusion depends on dual-mechanism which combines lamellipodia protrusion and purse-**

42 **string**

43 We monitored the actin organization at extruding cell-neighboring cell interfaces of laser-

44 induced apoptotic cells from Wild-Type (WT) and fluorescently-labeled actin MDCK cells

45 cocultured monolayers at high density (40-45 cells per 100 x 100 μm^2). Thin actin-labeled at

46 ruffled membrane indicated lamellipodial protrusions and were observed at the early time of

47 extrusion at the basal plane of neighboring cells in both WT/GFP-actin MDCK cells (Fig. 1a,

48 b) and WT/Ruby Life-act MDCK cells mosaic cultures (Supplementary Movie 1). Thick

49 bundles of actin indicating actomyosin cables were also formed in a non-uniform manner in

50 neighboring cells at the apico-lateral plane (Fig. 1a, b'). These partial apical actomyosin cables

51 were also observed during naturally-occurring extrusion (Supplementary Fig. 2b). We

52 validated the presence of lamellipodia by looking at cell extrusions in mosaic cultures of WT

53 and MDCK expressing YFP-tagged p21 binding domain (PBD), a fluorescent biosensor of

54 active Rac1 and Cdc42, [18, 19] for both laser-induced cell death extrusions (Supplementary

55 Fig. 1a, b) and naturally-occurring extrusions (Supplementary Fig. 2a). Enhanced PBD signal

56 in neighboring cells followed by directional cell edge movement towards the extrusion site

57 coincided with the rise of caspase-3 signal in the extruding cell (marked by caspase-3 indicator

58 DEVD-FMK), (Supplementary Fig. 1a & c-d, Supplementary Fig.2 a-a'), indicating that

59 lamellipodial protrusion emerged in response to apoptosis. This directional movement of

60 lamellipodia protrusion persists for a longer period than spontaneous lamellipodia fluctuations

61 unrelated to apoptosis that usually exist in the monolayer (Supplementary Fig. 1e-e'). We

62 observed similar processes at play for naturally-occuring and laser-induced cell extrusions

63 based on our established method [15]. In the following, we will present data based on laser-

64 induced extrusions to better control the initial conditions and ensure consistency between
65 analyses.

66   To further evaluate the influence of cell protrusions *versus* actomyosin cable
67 contractility, we looked at the evolution of the closing area defined by the edges of neighboring
68 cells as a function of time in basal and apico-lateral planes. Complete basal sealing beneath the
69 dying cells occurred in 30 min of extrusion (Fig. 1a), preceding apico-lateral area reduction
70 (Fig. 1d-d'). MDCK monolayers treated with the Rac1 inhibitor NSC-23766, which inhibits
71 lamellipodia formation, displayed delayed basal area reduction (Fig. 1e-e', Supplementary Fig.
72 3a), which was then concurrent with apical area closure. Rac1 inhibition also resulted in an
73 increased proportion of neighboring cells forming actomyosin cables (Fig. 1c) as well as in a
74 reduction of the number of successful extrusions (Fig. 1f). On the other hand, perturbing purse-
75 string formation with myosin II inhibitor - blebbistatin or formin inhibitor - SMIFH2 led to
76 increased lamellipodia presence and faster closure rate of the basal plane (Supplementary Fig.
77 3b-d). Nevertheless, all these inhibitors reduced the number of successful extrusions (Fig. 1f
78 & Supplementary Fig. 3b-d), indicating that extrusion was driven by combined effects of Rac-
79 induced basal protrusions and apical contractions of the neighboring cells.

80

81 **Rac1-mediated lamellipodia protrusions resulted in heterogeneous apico-lateral actin**
82 **organization**

83 In contrast to the expectation that a uniform, multicellular purse-string is prominent during
84 extrusion as proposed in previous studies [20], actin cables formed by surrounding cells were
85 instead non-uniform (Fig. 1a, Supplementary Movie 1, Fig. 2a). We then questioned the
86 contribution of such discontinuous actin cables to extrusion. We first quantified the
87 inhomogeneity of the actomyosin cable by measuring the intensity of myosin IIA
88 immunostaining at extrusion sites (Fig. 2a) and compared this parameter with or without the
89 Rac 1 inhibitor. Caspase-3 was used as the surrogate marker for the initiation of apoptosis and
90 stage of extrusion since the increase of caspase-3 levels as the function of time correlated with
91 the reduction in apical closing area (Supplementary Fig. 4a-a'). The inhomogeneity in
92 actomyosin II staining cable decreased with the intensity of caspase-3 (Fig. 2b; Supplementary
93 Fig. 4b). Myosin distribution was only uniform at the final stage when the caspase-3 signal was
94 maximum (Fig. 2b). We also quantified the inhomogeneity of actin distribution as a function
95 of extrusion area and confirmed that inhomogeneous actomyosin cables persisted at

4

96 neighboring-extruding cells interface until the end of extrusion (Fig. 2d-f; Supplementary Fig.
97 5a).

98   We rationalized that the purse-string may not need to span all cells to exert contractility:
99 the actomyosin cables accumulated at each neighboring cell-extruding cell junctions could still
100 contract. To test this hypothesis, we measured and cross-correlated the length of each junction
101 as the function of time with its actin intensity over time (Fig.2f, Supplementary Fig. 5a-c). At
102 the interfaces which form actin cables, the intensity of actin accumulation at these junctions
103 correlates with junction's shortening (Supplementary Fig. 5b). Such correlation for junctions
104 that form cables was higher when compared with junctions that do not form actin cables
105 (Supplementary Fig.5b'-c, Fig. 2f). This result supported that contractile activity occurred at
106 the individual junction level over the time-course of extrusion. This persistence of
107 discontinuous purse-string is opposite from the view that a complete actomyosin ring is
108 required for junctional reductions in neighboring cells.

109   As perturbing lamellipodia protrusion by NSC-23766 led to simultaneous reduction of
110 basal and apical extrusion area (Fig. 1e-e'), we questioned the impact of lamellipodia formation
111 on the assembly of actomyosin cables. We found that inhibiting lamellipodial extensions by
112 NSC-23766 treatment led to a more uniform distribution of Myosin II (Fig. 2a-e). Also, this
113 uniform distribution of Myosin-II in NSC-23766-treated cells was independent of the caspase-
114 3 levels (Fig. 2b). Even when actomyosin distribution became homogeneous and formed
115 complete purse-strings around the apoptotic cell, these purse-strings were typically tilted in z
116 over several μm (Fig. 2g-g'). These actomyosin rings were tilted $31.6^o \pm 10.0^o$ with respect to
117 the horizontal plane, while they were typically more horizontally oriented $10.5^o \pm 2.8^o$ in NSC-
118 23766 treated monolayers (Fig. 2h). Therefore, lamellipodia protrusion might elicit the
119 heterogeneous actomyosin organization during extrusion.

120   We postulated that the tilting of the full ring at the end stage of extrusion was due to
121 two factors: non-uniform formation of contractile actin cables at apical levels and lamellipodia
122 protrusions that delay myosin enrichment to form contractile cables. The representative
123 example on Fig.1a illustrates further this point. As cell extended lamellipodia (Fig.1a, cell #1,
124 top view and side view), the interface shared with its neighbors followed cell body extension
125 and thus localized at the basal plane. This results in cell #2, #3, the side cell #4 connected to
126 #3 being pulled to the basal plane. However, without lamellipodia protrusion, the rest of cell
127 #4 remained at apical plane (18 min) when it started to form actomyosin cable. As a

128 consequence, the actomyosin ring observed at late stages was partly connected to the basal part.

129 To further support this model, we imaged cells co-expressing TdTomato F-Tractin and Myosin

130 Regulatory Light Chain (MRLC) to distinguish actin at contractile cables and actin-

131 accumulated at protrusive membranes (Supplementary Fig. 6, Supplementary Movie 2). Actin

132 protrusion at the basal sides was observed first, followed by myosin enrichment at the same

133 plane and myosin reduction at 1-2 µm above, suggesting that basal protrusion helped to anchor

134 actomyosin cables in the apical-to-basal direction.

135 These findings evidenced that lamellipodia protrusions preceded and caused

136 heterogeneous patterns of actomyosin cables formation. As lamellipodial protrusion is

137 stochastic, the resulted purse-string ring is heterogeneous, as observed. Early basal sealing was

138 accomplished by lamellipodial protrusions, and extrusion is completed through apical closure

139 by purse-string, which can either be partial or uniform. Failure of extrusion in the case of

140 lamellipodia inhibition implied that such a sequence of events was more important than a

141 single, uniform purse-string formation.

142

143 **Modulation of cell-cell junction strength dictates the dominant mechanism of extrusion**

144 As partial actomyosin cables persisted during extrusion, we next questioned whether the

145 presence of a full purse-string ring was dispensable for cell extrusion. In oncogenic extrusion,

146 remodeling of E-cadherin followed by a redistribution of junctional tension was sufficient to

147 drive extrusion without a prominent purse-string ring [11, 13, 21]. Adherens junctions have

148 also been reported to mediate the rearrangement of cells surrounding the extrusion site [12]

149 and the formation of contractile actin cables [14]. Our experiments showed that junctional

150 complexes between extruding and neighboring cells were remodeled. The reduction of

151 junctional E-cadherin between extruding and neighboring cells was observed at the middle

152 stage of extrusion (Supplementary Fig. 7a, 60 min, middle panel, white open arrows,

153 Supplementary Fig. 7c, 78 min) in a non-uniform manner. Subsequently, inhomogeneous

154 accumulation of active RhoA (Supplementary Fig. 7a-b) were observed. These sequences of

155 events where molecular regulators of cellular tension assemble in a non-uniform fashion recall

156 the partial actomyosin purse-string formation described so far.

157 We thus examined the contribution of cadherin-catenin complexes to cell extrusion by

158 analyzing extrusion in α-catenin knocked-down (αcatKD) MDCK cells fully deficient for

159 adherens junction (AJ) formation. We imaged actin distribution at extrusion sites (Fig. 3).

160 Extrusion of these cells entirely engaged the lamellipodia-based mechanism (Fig. 3a, a'), and
161 as a result, apical closure was strongly delayed compared to basal closure (Fig. 3b-b').
162 Occasionally, we observed the accumulation of actin at the apical plane for αcatKD cells facing
163 the extruded cells (Fig. 3a, 30 min). To exclude the possibility that this accumulation of actin
164 was part of functional contractile actomyosin cables, we performed laser ablation on these
165 myosin- enriched interfaces and followed the associated junctional recoil (Fig. 3c-f). Laser
166 ablation in αcatKD cells induced junctional recoil twice slower than the one observed in WT
167 cells (Fig.3d-e). Besides, initial recoil velocity of the ablated junction in αcatKD cells during
168 extrusion was independent of junctional myosin accumulation, in contrast to the linear increase
169 in WT case (Fig.3f). These results indicated that weakened cell-cell junction (CCJ) in αcatKD
170 cells caused impaired purse-string contractility.

171 To artificially create a condition with different CCJ strength in between dying cell and
172 neighboring cells, we co-cultured WT and αcatKD MDCK cells and induced apoptosis in WT
173 cells, which were surrounded by both WT and αcatKD cells. We found that neighboring
174 αcatKD cells, with weakened CCJ engaged in extrusion could switch to lamellipodia-based
175 protrusion and participate in basal closure (Fig. 4a-b), while neighboring WT cells formed
176 contractile actin cable (Fig. 4a, top panel). In these mosaic monolayers, the αcatKD cells
177 displayed faster basal cell edge movement towards the extrusion center than WT cells (Fig.4b).
178 This set of experiments confirmed that cells with weaker CCJ strength at the interface with the
179 extruding cell used lamellipodia protrusion as the dominant mechanism.

180 We further proved that by varying CCJ strength using cells expressing various α-catenin
181 mutants that could either reduce or enhance CCJ strength [22-24], we could tune the
182 mechanism of extrusion. The expression of these different α-catenin mutants into αcatKD cells
183 (see Method section) rescued the contribution of actomyosin cables with different degrees
184 (Fig.4c, Supplementary Movie 3). αcat-L344P expressing cells, unable to recruit vinculin at
185 CCJs despite being unable to form actin cables (Supplementary Movie 3), formed pronounced
186 lamellipodial protrusions around extruded cells. In contrast, cells rescued with αcat-WT or
187 αcat-ΔMod (constitutively recruiting vinculin) constructs formed more pronounced actin
188 cables around extruded cells (Supplementary Movie 3). αcatKD MDCK cells, which formed
189 lamellipodial protrusions closed the basal area faster than the other mutants, while αcat-ΔMod
190 cells, which preferentially formed purse-string, displayed the most delayed basal area closure
191 (Fig.4d-e). This further validates that cadherin-mediated adhesions were crucial to modulate
192 cell protrusion and actin cable activities during extrusion. Although either reducing or

193   enhancing CCJ strength altered basal closure timing, it did not affect the duration of extrusion,

194   as followed by apical closure timing (Fig.4f). These data indicated that on substrate with

195   homogeneous adhesion, monolayers with altered CCJ strength could adjust the relative

196   contribution of lamellipodia protrusion/purse-string to successfully extrude dying cells.

197

198   **Basal lamellipodia protrusion controls cell extrusion via cell-substrate adhesion assembly**

199   We further investigated the contribution of lamellipodia protrusion to ensure successful

200   extrusion. The inhomogeneity of actomyosin cables at the apical plane was suggested to be the

201   result of lamellipodia protrusion at the basal part, implicating the role of cell-matrix adhesion

202   in the formation of these cables. Therefore, we aimed to decouple lamellipodia protrusion and

203   actomyosin cable contractility by manipulating cell-substrate adhesion. We cultured MDCK

204   monolayers on micro-patterned substrates containing non-adhesive circular patches, and laser-

205   induced apoptosis on cells sitting on top of these patches. We varied the size of the patches

206   from 10 μm to 30 μm in diameter to cross-over subcellular and cellular dimensions and, thus,

207   partially or entirely prevent cellular protrusions of the neighboring cells.

208   Mechanical inhibition of cell protrusions by the non-adhesive patch (diameter = 30 μm)

209   resulted in isotropic actin cable formation (Fig. 5a, Supplementary Movie 4). Continuous

210   recruitment of actin cables to the purse-string appeared to pull on cell-cell junction (CCJ) as

211   revealed by the accumulation of E-cadherin at the tips of surrounding CCJs (Fig. 5a, arrows,

212   Supplementary Movie 4). The purse-string was also composed of radial cables, which

213   emanated out of the continuous tangential cables, connecting to focal adhesion complexes at

214   the edges of the non-adhesive patterns (Fig. 5b, white open arrow & Supplementary Fig.8a &

215   d) as previously observed during collective cell migration [25]. Some cables connect the focal

216   adhesion with cell-cell junction (as visualized by enhanced actin at junction, pointed by a pair

217   of cyan arrowheads in Fig. 5b). These observations revealed that the actin meshwork formed

218   in response to extrusion was not only supported by multicellular actomyosin cable anchored

219   across cell-cell junctions but also emerged from cables connected to cell-substrate adhesions.

220   Laser ablation performed on these radial cables resulted in the recoil of both the purse-string

221   (Supplementary Fig. 8a, b & b', initial recoil velocity = 0.13 ± 0.01 μm/s) and the rear of the

222   cell away from extrusion site (Supplementary Fig. 8a, c & c', initial recoil velocity = 0.07 ±

223   0.01 μm/s) indicating that these cables are under tension.

224   In agreement with our data on pharmacological inhibition of lamellipodia (Fig.1e-e'),

225   the uniform purse-string alone was not sufficient to extrude apoptotic cells at 30 μm diameter

226   non-adhesive patches (Fig. 5a, Supplementary Movie 4). The dying cell detached from its

227   neighbors without the simultaneous sealing activity from the neighbors (Fig. 5a,

228   Supplementary Fig. 9a, Supplementary Movie 4). To investigate the extent to which the lack

229   of substrate adhesion impeded extrusion we varied the non-adhesive patch size (Fig. 5c and

230   Supplementary Fig. 9). A monotonic trend was observed between the patch size and extrusion

231   efficiency (Fig. 5c, Supplementary Fig. 9b-b'), supporting that by forming nascent focal

232   adhesion, protrusions from neighboring cells control the formation of purse-string to extrude

233   the dying cells.

234

235 Deconstructing the mechanical forces of cell extrusion using micropatterned surfaces

236 As both lamellipodia protrusion and actomyosin cables can exert mechanical forces [16, 17,

237 26], we sought to understand how these forces contribute to successful extrusion. Therefore,

238 we further dissected the mechanical work contribution by lamellipodia versus purse-string.

239 Traction force cells exerted on the substrate has been used to describe forces generated by both

240 lamellipodia and purse-string during wound healing processes [16, 25]. These studies shown

241 that during wound healing, lamellipodia exert traction forces pointing radially and away from

242 the wound center, while purse-string traction forces are generally tangential or radially inwards.

243 We thus adapted traction force microscopy to dissect the relative forces contributed to these

244 two mechanisms during extrusion. We observed an increase of the overall traction forces upon

245 cell extrusion as compared to forces at random sites (Supplementary Fig. 10 a-b). By

246 decomposing forces into radial and tangential components, we concluded that both components

247 played a role in the force increase (Supplementary Fig. 10c), exhibiting an anisotropic

248 distribution of forces at extrusion sites. Furthermore, the observation of inward- and outward-

249 pointing forces with respect to the center of the extrusion zone suggested that both mechanisms,

250 lamellipodia protrusion and purse-string, contributed significantly to cell extrusion, in

251 agreement with previous studies on wound healing and epithelial gap closure [16, 25]. As

252 extrusion progressed, the purse-string mechanism appeared more pronounced (Fig.1a,

253 Supplementary Fig. 10a) reflected by a more prominent contribution of inward-pointing forces

254 (Supplementary Fig. 10a).

255 To further investigate the relative mechanical contributions of the two mechanisms at

256 play during extrusion, we first measured the forces during extrusion over circular (10, 15, and

257 30 μm-diameter) non-adhesive patches to determine the forces produced by purse-strings. The

258 fact that contractile purse-string is partially connected to the focal adhesions at the edge of the

259 patch indicates that the resulting forces generated by purse-string could be measured by traction

260 force exerted on the edges of non-adhesive patches. Indeed, pronounced traction forces were

261 observed at the edges of the non-adhesive patches during extrusion (Fig.5d). These forces are

262 prolonged for 2.5 hours on patches of D = 30 μm and 15 μm corresponding to incomplete

263 extrusion on these patches. On 10 μm diameter non-adhesive patches, the forces diminished

264 after 60 minutes (the duration when extrusion is typically completed). Also, on D = 10 μm the

265 orientation of force was more anisotropic (Fig. 5e iii & Supplementary Movie 6) compared to

266 prominent radial inwards-pointing forces observed on 15 μm and 30 μm diameter non-adhesive

267 patches (Fig. 5e-i & ii, Radial Traction Force & Orientation of the forces with respect to

268 extrusion center, Supplementary Movie 7). The dependence of the force pattern on the non-

269 adhesive patch diameter corroborated with the reduced contribution of lamellipodia to

270 extrusion as the patch size increased.

271 We estimated the tension contributed by purse-string using force measurement on non-

272 adhesive patch of D = 30 μm. We represent the contractile force exerted by purse-string by the

273 line tension γ (the radial traction force divided by radius of extruding cell). On non-adhesive

274 patch of D = 30 μm, we observed that total and radial forces diminished together with the re-

275 opening of the closing area during extrusion (Fig. 5d-i & e-i, Supplementary Fig.11a). For the

276 total work done to move the cell edge across the non-adhesive area of radius R, without

277 lamellipodia protrusion, the radial traction force F_{radial} needs to be large enough to generate the

278 work to overcome the resistivity of the bulk: $dW_{radial} = F_{radial}.dr \geq \gamma.(2\pi R).dr$. At non-adhesive

279 patch size of D = 30 μm, F_{radial} is only contributed by purse-string. Since extrusion always fails

280 on this size, we could estimate the force exerted by purse-string by identifying the range at

281 which the Work dW changed sign (corresponding to the re-opening of the closing area, range

282 between the dashed line on Supplementary Figure 11a). As such, we estimated that the tension

283 by purse-string was γ = 6.5 ± 1.4 nN/μm (a value consistent with the value reported in [25])

284 (Supplementary Fig. 11a, middle panel).

285 The estimation for purse-string tension was validated again on extrusion on non-

286 adhesive patch size of D = 15 μm (Supplementary Fig. 11b). Note that at the range γ = 6.5 ±

287 1.4 nN/μm, the purse-string produces non-zero Work and as such, extruding area is reduced

288   linearly before reaching flat ends. On patch size of D = 10 μm, we observed that the F_{radial} only

289   started increasing (Supplementary Fig.11c – middle panel) at T = 40 min, corresponding to a

290   radius around 2-2.5 μm. Since the non-adhesive patch remained smaller than the typical cell

291   size, we expected that lamellipodia-based forces could contribute to cell extrusion over larger

292   time scales than in the previous cases, leading to a delayed signal in solely purse-string based

293   forces (Supplementary Fig. 11c).

294   We further investigated how cell-cell junctions strength modulated the forces

295   contributed by purse-string during extrusion. We combined non-adhesive patches with the

296   αcatKD, αcat-L344P and αcat-ΔMod cell lines of varying CCJ strengths. We compared their

297   behaviors on non-adhesive patches with diameters of 10, 15, 20, 25 and 30 μm with those of

298   WT cells (Fig. 6). αcatKD cells failed to be extrude successfully from the non-adhesive patchs

299   even at small sizes (Fig. 6a, Supplementary Movie 8). We also estimated the line tension

300   produced by actin cables formed by αcatKD cells to be less than 1 nN/μm (Supplementary Fig.

301   11d). Although there was actin accumulated around the extruding-neighboring interfaces and

302   caspase-3 signal was elevated, the extruding area stagnated over 6 hours. In αcat-L344P cells,

303   the actomyosin cables were observed at CCJ as the extruding area reduced (Fig.6b). However,

304   most of the extrusions failed in this case because the actin cable was not sustained (Fig. 6b).

305   On the other hands, extrusion of αcat-ΔMod cells was generally successful with visibly

306   actomyosin cable reinforcement (Fig.6c, white arrowheads). Furthermore, there were also

307   successful extrusions for these cells on larger non-adhesive patches (Supplementary Movie 9).

308   In summary, enhancing CCJ strength could increase the speed of closure on non-adhesive

309   patches (Fig. 6d-e).

310   Finally, previous studies have shown that substrate curvature can promote either

311   lamellipodia-based protrusions or actin cable assembly [17, 25]. Along this line, we developed

312   anisotropic patterns (Fig. 7) with a positive curvature side which could favor lamellipodia

313   protrusion and a negative curvature side which could favor actin cable formation [17, 25].

314   Preferential formation of a cable at the negative-curvature before the formation of actin cable

315   on the positive-curvature was observed (Fig. 7a). At the positive curvature side, lamellipodia

316   protrusion was dominant until the protruding front reached the edge of the patch and converted

317   into actin cable (Fig. 7a, t = 12 min and t = 18 min, white arrowhead). The forces generated by

318   lamellipodia protrusion and actomyosin cables were also dissected on these anisotropic non-

319   adhesive shapes (Supplementary Fig. 12). As extrusion progresses, higher radial traction forces

320   pointing towards the center accumulated at the negative edge than at the positive edges while

321 the overall traction forces increased around the shape's edges (Fig. 7b & c). On positive

322 curvature, outward-pointing traction forces span the patch edge during early extrusion (Fig. 7d

323 & f, Supplementary Fig. 12a & b, top panel, 0-30min), that were attributed to the forward cell

324 crawling movement. The force orientation became tangential to the edge of the cell as it

325 crawled towards the edge of the non-adhesive patch (Supplementary Fig. 12a & b, top panel,

326 45min). On the negatively curved region of the patch, forces oriented tangentially to the cell's

327 edge (Fig. 7d' & f', Supplementary Fig. 12a' & b', 45-72 min). Over time, cells were pulled

328 inside the non-adhesive area, leading to a change of force patterns with an increase of inward-

329 pointing forces (Supplementary Fig. 12, 87 min, Fig. 7 e-g). It could be explained by the

330 formation of cables that linked cellular front over the non-adhesive area to remaining adhesions

331 at the back (Fig. 7a, 108 min). Altogether, these data helped to clarify the force pattern and the

332 mechanical signature of the transition associated to lamellipodia and actin cable assembly.

333

334 A theoretical model to reconcile forces produced by purse-string and lamellipodia

335 protrusion during extrusion

336 In order to provide an integrated view of the extrusion mechanism driven by cell protrusions

337 and contractility, we developed a theoretical model. In two recent works, a theoretical

338 framework emerged to account for the high variability in the completion time of wound [24,

339 25]. In spite of similarities, including in terms of time scales, the length scales involved in

340 extrusion are significantly lower than in the wound closure experiments reported in [24, 25],

341 indicating discrepancies in the strength of the forces involved in these processes. Our

342 theoretical model reconciled the relevant forces involved in extrusion and wound closure, as

343 well as the two experimental features observed here in the context of extrusion over adhesive

344 and non-adhesive substrates (see Fig. 8a-d).

345   In the adhesive case, we expect basal lamellipodia protrusions to generate forces

346 oriented towards the extruding cell; such contribution to the tissue spreading dynamic

347 corresponds to a negative isotropic stress contribution that drives a full extrusion for any initial

348 size of the ablated cell. As such, the stress exerted at the boundary between neighboring cell-

349 extruding cell can be written in terms of a boundary stress equation $\sigma_{r=R(t)} = P_c + \sigma_P + \sigma_\mu +$

350 $\frac{\gamma}{R(t)} + \xi$ (Supplementary, Theoretical Appendix, Eq. 4) where R(t) is the radius of the closing

351 area; P_C is the overall monolayer prestress; σ_P is the protrusive force the neighboring cells

352 exerted at the interface ($\sigma_P > 0$ for lamellipodia protrusion [27, 28]); γ is the tension along

12

353   the actomyosin cables within the multicellular purse string located on the apical side; ξ

354   encompasses different sources of short-time scale stress fluctuations, generated either along

355   the acto-myosin cables or within the bulk of the tissue; finally, we introduce a term σ_μ to

356   account for the stress exerted through radial actin cables, providing a resistive contribution to

357   extrusion ($\sigma_\mu < 0$) in the case of non-adhesive patches.

358   Solving the equations for $R(t)$ as the function of time (Eq.7-11), we found that the

359   completion time for the adhesive substrate is largely independent of the value of the

360   contractility by the actomyosin cable. This is consistent with our experimental results that

361   modulating actomyosin cables contraction *via* changing CCJ strength does not significantly

362   alter the duration of extrusion (Fig.4f).

363   The difference in the non-adhesive case lies in the existence of radial stress fibers that

364   spread from the edges of the non-adhesive patch (basal side) to the edge of the tissue (apical

365   side, see Fig. 5b, Fig.8c-d, Supplementary Fig. 8d). As they were shown to be tensile

366   (Supplementary Fig. 8a-d'), these radial cables resist the closure activity of neighbors. These

367   fibers become increasingly tilted in the apico-basal direction (Fig.8d, Supplementary Fig. 8d'),

368   and these angles are correlative to the strain exerted when closure occurred on non-adhesive

369   patches (Supplementary Fig. 8e). Taking into these observations, we consider the simplest

370   assumption of constant contractility along these fibers. In turn, the projected in-plane tissue

371   stress is an increasing function of the tilt; hence it increases during the extrusion process (see

372   Supplementary Note – Fig. 1). We experimentally showed that the cell extrusion failed

373   whenever the size of the non-adhesive patch is bigger than a critical radius, which can be

374   estimated by numerical simulation (see Theoretical Appendix- Fig.SI Theory Fig.2).

375   By considering the stress fluctuation ξ in Eq.5 as the function of R, which depends on

376   fluctuation by pressure, purse-string and apical-basal cables, we show that these fluctuations

377   do contribute to closure of extrusion site (Supplementary Note - Eq.10 and Eq.11). We used

378   numerical simulation to solve the probability of extrusion as the function of initial size and

379   probability according to this framework. We compared our simulation with experiments

380   performed with cells expressing different αcat mutants (Fig.8e-f) on different non-adhesive

381   patch sizes. The trend obtained from numerical solutions varying the strength of the purse-

382   string contractility (see Fig.8e-f) closely follows the trend observed in experiments with

383   different αcat mutant background for cells on non-adhesive patches. Our analytical model

384   demonstrated that the presence of fluctuations may lead to the completion of the extrusion

385   process, even in a phase space of parameters where deterministic forces would prevent it from
386   occurring. It also suggests that α-catenin may not just reduce the overall contractility, but also
387   the level of contractility fluctuations.

388

389   **DISCUSSION**

390   Our experimental and theoretical findings establish a new quantitative scenario for the
391   mechanisms driving cell extrusion in an epithelial sheet. It provides a holistic model of the joint
392   efforts of two distinct cellular processes, lamellipodia protrusions and contractile actomyosin
393   cables to eliminate apoptotic cells from tissues while maintaining epithelial integrity. Branched
394   actin networks of lamellipodia provide fast pushing forces on the membrane to close the
395   extruding area early at the basal plane. Contractile actomyosin cables first form at apical planes
396   in a discontinuous manner only become uniform at later stages of extrusion. Lamellipodia
397   assembly leads to protrusive activity underneath the dying cell but also helps to anchor
398   actomyosin cables in apical-to-basal direction. Hence, the tilted localization of the complete
399   purse-string rings shows unanticipated closure processes, which are following not only
400   horizontal but also apico-basal directions.

401   The dual-mechanism mode involving lamellipodia protrusion and heterogeneous purse-
402   string could be adjusted by changing cell-substrate adhesion patterns or AJ strength. Such
403   dual-mechanism ensures that basal sealing is accomplished and further maintains epithelial
404   integrity during apoptotic extrusion. Our results provide additional models besides the ones
405   already published [5, 7, 29], which emphasized the dominant role of a complete multicellular
406   purse-string that fully surrounds the apoptotic cell during extrusion.

407   The combined effect of lamellipodial protrusions and actomyosin contractility during
408   extrusion is well captured by the observed force patterns and our theoretical approach. We
409   delineated the efficient forces exerted by the purse-string or lamellipodial protrusions that
410   should overcome the bulk resistance of the epithelial monolayer by both experimental traction
411   force analysis and the analytical model. We were able to deconstruct experimentally the force
412   values for lamellipodia and purse-string during extrusion. The purse-string formation results in
413   forces pointing radially towards the center of extruding cell on top of non-adhesive patches as
414   extrusion progresses (Fig. 4e) with a measured line tension of 10-13 nN. These force
415   magnitudes corroborate with those measured on large wound closure [16, 17, 30]. The
416   estimated stress exerted by lamellipodial protrusions was between 50-100 Pa, in agreement

14

417   with previous measurements [15, 31]. By theoretical modeling and comparing the numerical

418   solution with experimental data, we unveiled the relative contributions of forces at play to expel

419   dying cells from epithelial monolayers.

420   Heterogeneous mechanisms have been proposed to facilitate wound healing and gap

421   closure [16, 17, 32, 33]. These studies emphasized that the full, uniform purse-string was

422   important yet sometimes not sufficient to promote gap closure. Recent *in silico* studies

423   suggested that a mixed mechanism of contractile purse-string and protrusive crawling were

424   more efficient than single-mechanism-based closure [34, 35]. Similarly, experiments done in

425   this work prove that a dual-mechanism is essential for cell extrusion. We provide further

426   information on how lamellipodia-driven basal protrusions could affect subsequent purse-string

427   formation three-dimensionally. This is strikingly different from the case of wound closure

428   since, in extrusion, the closing activity is coupled with partial apico-basal changes when the

429   extruding cell gradually loses contact with its neighbors. In wound healing, actin reorganization

430   at the front of the wound only occurs in two dimensions.

431   The heterogeneous changes of actin structures around the extrusion site were found to

432   be coupled with the non-uniform remodeling of CCJ between the extruding cell and its

433   neighbors. Previous studies showed that the reduction of E-cadherin at the junctions, together

434   with a reduction of tension at the lateral membrane, occurs before extrusion [6, 11, 36]. The

435   reduced tension at the CCJs is necessary for increased contractility that expels the cell [11],

436   and redistribution of E-cadherin clusters is crucial to recruit factors organizing actomyosin

437   purse-string like Coronin 1B [14]. Here we provide an additional role of AJ in mediating

438   extrusion via dual-mechanism mode. The stochastic formation of lamellipodia at early

439   extrusion stages led to an asymmetrical partial loss of apico-basal polarity and reduction of AJ

440   at each neighbor-extruding cell interfaces, which corresponds to inhomogeneous actomyosin

441   purse-string formation. Furthermore, while cadherin-catenin complexes are reduced at

442   bicellular interfaces, they appear to be enhanced at tricellular contacts together with the

443   recruitment of actomyosin cables, suggesting that there is likely positive feedback between AJ

444   reinforcement and actomyosin cable maintenance.

445   Taken together, we established the interplay of the cell-cell junction and cell-substrate in

446   regulating the extrusion mechanism by tuning lamellipodia protrusion and contractile purse-

447   string mode. The switching mechanism from lamellipodium protrusion to contractile purse-

448   string helps epithelia adapt to the environment with heterogeneous substrate adhesion

449 molecules, which typically occurs *in vivo* to maintain homeostasis**.** The complex and

450 heterogeneous regulation, even at a small-scale event, epitomizes the robustness of epithelia

451 and proposes a new framework for understanding epithelial homeostasis as well as extrusion-

452 related pathological conditions.

453

MATERIALS AND METHODS

Cell line and tissue culture

Madin-Darby canine kidney (MDCK) strain II was cultured in DMEM medium (Invitrogen) supplemented with 10% FBS (Invitrogen). To study the function of specific proteins, stable cell lines or transient expression/knock-down variant of MDCK were used. Stably transfected cells including GFP-actin MDCK, Lifeact Ruby MDCK, α-catenin knock-down MDCK, mCherry E-cadherin MDCK, and GFP E-cadherin MDCK are kind gifts from James W. Nelson. MDCK PBD-YFP expressing MDCK was kindly provided by Fernando Martin-Belmonte, Universidad Autónoma de Madrid. These stably-transfected cells are maintained with media supplemented with 250 µg/mL geneticin (Invitrogen) to maintain their gene expression. Fluorescence-labeled cells are checked regularly for uniform fluorescence intensity and selected by cell sorting if necessary. Mycoplasma test was done every three months to control the mycoplasma contamination.

Plasmids and transfection

To study the role of CCJ during extrusion, we manipulated α-catenin expression. The α-catenin mutants were published previously [22]: L344P mutant with the leucine to proline point mutation at the 344aa of VH2 domain conferring α-catenin's inability to bind to vinculin, and Δ-Mod mutant which has the vinculin-binding modulatory domain deleted (aa 396-631) and allows α-catenin to be constitutively bound to vinculin. These mutant constructs were transiently transfected in α-catenin knock-down MDCK cells to generate cell populations with varied CCJ strength. In this study we used: α-catenin knock-down (αcatKD), α-catenin L344P (L344P), wild-type α-catenin (WTres), α-catenin Δ-Mod (ΔMod). mEmerald-MyosinIIA-N, mApple-Actin, GFP-Actin, mCherry-ARPp34-N were kindly shared by Pakorn Kanchanawong. GFP-APHP RhoA sensor was the generous gift from Alpha Yap. Transfection was performed with Neon electroporation system (Invitrogen).

Laser Induction System to study apoptotic extrusion

We induced apoptosis in monolayer by UV laser to be able to capture early events of extrusion. The system was designed as in [37], consisting of a Nikon A1R MP laser scanning confocal microscope, with Nikon Apo 60 X oil-immersion/1.40 objective. To induce apoptosis, UV-laser (355nm, 300 ps pulse duration, 1kHz repetition rate, PowerChip PNV-0150-100, Teem Photonics) was focused at the target cell for 7-10s with the power of 10 nW at the back aperture. With this setting, DNA-strand break is induced without permeabilization of the membrane [15]. This induces cell undergoing apoptosis and being extruded.

Cell Seeding Setup

To distinguish lamellipodial protrusion and actin cable formation at the extruding cell neighboring cells interface, we used mosaic cocultures of non-fluorescent cells (which would be laser-induced for apoptosis) and fluorescence-labeled GFP-actin or Lifeact Ruby cells at the ratio of 1:7. Cells were trypsinized, mixed and seeded at 2×10^6 cells/µm^2 on glass bottom petri dish (Iwaki) coated with fibronectin (Roche, 1hour incubation, 25 µg/mL) or on fibronectin-micropatterned substrates. 16-20 hours before imaging. Cell attachmente was monitored every half an hour and unattached cells were washed by PBS. Cells density was kept at the range of 40-45 cells per 100 x 100 µm2 unless otherwise specified for density-dependent measurements.

Determination of extrusion initiation (t= 0 min)

17

498 Initiation of apoptotic extrusion was defined by (i) the brightening of caspase-3 indicator, (ii)
499 a bright spot on phase contrast or bright field image, (iii) the sharp shrinkage of the cell area
500 and (iv) the initiation of nucleus condensation and fragmentation. Our previous published
501 results indicate that these four hallmarks occur simultaneously within the time interval of
502 interest (3-5min) followinglaser induction pulse [10].

Drug Treatment

504 Drugs were incubated 2 hours prior to imaging unless stated otherwise. The drug
505 concentrations are as follow: (S)-nitro-blebbistatin (Cayman Chemical) 50 µM, NSC-23766
506 (Sigma-Aldrich) 200 µM, SMIFH2 (Sigma) 50 µM dissolved in DMSO. Caspase-3 indicator
507 DEVD-FMK conjugated to Sulfo-rhodamine (Abcam) was used at 1:1000 dilution and
508 incubated with the cells 30 min before experiment. To visualize F-actin in certain experiments,
509 siR-actin (Cytoskeleton) was added at 100 nM concentration to the medium 12 hours before
510 imaging. Hoechst 33342 at 1µg/mL (Sigma) was added into culture media 1 hour and washed
511 before imaging for nucleus live detection.

Micropatterning of the substrate

513 Wafers with the custom-designed patterns and micropillars were prepared following
514 photolithographic techniques as described previously [38].

515 For cell monolayer confined on patterns, a stenciling technique was used. PDMS (Sylgard 184,
516 Dow Corning) was mixed with crosslinking agent to the ratio of 10:1. The mixture was poured
517 onto the wafer and degassed then cured at 80°C for 2 hours. The stencil with patterns of interest
518 was deposited onto the glass-bottomed IWAKI dishes and plasma-treated with Oxygen for 30
519 minutes. By this way, the non-patterned area on glass surface became functionalized and could
520 attach to 0.1 mg/mL PLL-g-PEG (SuSoS) that was flowed in later by capillary. The dish was
521 incubated with PLL-g-PEG for 1 hour before removing the stencil and coated with fibronectin.
522 Fibronectin was washed off and the surface was further treated by 2% pluronics (F127, Sigma)
523 for further passivation of non-patterned area.

524 For experiments with non-adhesive patches, micro-contact printing was used instead of micro-
525 stenciling. PDMS substrate was spin-coated at 1000 rpm for 30s then 4000 rpm for 30s on
526 IWAKI petri dishes and cured for 1.5 hours at 80°C. PDMS stamps were prepared from wafer
527 molds and coated with mixture of 50 µg/mL fibronectin (Roche) and 25 µg/mL Atto647-
528 conjugated fibronectin (Atto dye, Sigma). Stamps were deposited on deep UV-treated surfaces
529 (15 min) and the unstamped areas were passivated by 2% pluronics (F127, Sigma) for 2 hours
530 to render non-adhesive surface. The dishes were rinsed with PBS three times before seeding
531 cells.

Immunostaining and antibodies

533 Cells were fixed with 4% PFA at 37°C for 10 minutes, permeabilized and blocked with 0.1%
534 Triton X-100 in 1% BSA/PBS overnight. Myosin IIA was stained using rabbit Anti-myosin
535 IIA antibodies (Sigma M8064) 1:100. Paxillin was stained using rabbit monoclonal anti-
536 paxillin antibodies [Y113] (Abcam ab32084) 1:100. Actin filaments were stained with Alexa
537 Fluor® 568 Phalloidin (Life Technologies) 1:100, Alexa Fluor® 488 Phalloidin (Life
538 Technologies) 1:100 or Alexa Fluor® 647 Phalloidin (Life Technologies) 1:100. Secondary
539 antibodies Goat Anti-rabbit IgG Alexa Fluor® 568 (Life Technologies) were used at a 1:100
540 dilution. Nucleus was labeled with Hoechst 33342 at 1µg/mL concentration.

Microscopy

Time-lapse confocal imaging was carried out with spinning disk confocal microscopy (Nikon Eclipse Ti-E inverted microscope body, CSU-W1 Yokogawa head, dichroic filters and 1.27 NA 60X water-immersed objective). GFP fluorescent signal was taken with 488 nm Diode laser, 50 mW, 5% power, 100 ms exposure. RFP/mCherry/mApple fluorescent signal was taken with 561 DPSS laser, 25 mW, 5% power, 100 ms exposure. Images were taken with z step = 0.5 μm, 17-19 stacks. Super-resolution imaging was done using the Live-SR module (York et al., 2013) integrated with the above-mentioned spinning disk confocal microscope using a 1.6 NA 100X oil-immersed objective. GFP fluorescent channel was taken with 488 nm Diode laser, 50mW, 8% power, 100 ms exposure. RFP/mCherry/mApple fluorescent signal was taken with 561 DPSS laser, 25 mW, 10% power, 100 ms exposure. DAPI fluorescent channel was acquired with 405 nm Diode laser, 50 mW, 5% power, 100 ms exposure. Images were taken with z step = 0.1 μm. Microscope settings were kept constant throughout the set of experiments for keeping consistent quantification.

Traction force microscopy

For traction force microscopy, a substrate of 10-20 kPa Young's Modulus was prepared by mixing CyA and CyB PDMS components (Dow Corning) at the ratio of 1:1 to enable detection of nanoNewton forces. The mixed PDMS was spin-coated onto glass-bottomed petri dishes (IWAKI) and cured in 80°C for 30 minutes. The surfaces were then incubated with 5% (3-Aminopropyl)trimethoxysilane (Sigma) in ethanol for 5 min. carboxylated red fluorescent beads (100 nm, Invitrogen) were then functionalized on the substrate at a 1:500 dilution in deionized (DI) water. The beads were passivated with 100 mM Tris solution (Sigma) in DI water at for 10 min. Finally, fibronectin (50 μg/ml) was incubated for 1 hour at 37 °C. This substrate was patterned on soft gel using indirect micro-contact printing. First, the pattern of interest was stamped first on thin Polyvinyl Alcohol membrane made up of 5% PVA solution (Sigma) and transferred the inverted membrane to the substrate. The membrane was dissolved, and the non-patterned areas were passivated by incubation with 2% Pluronics for 2 hours. Finally, cells can be seeded onto the substrate as previously described.

The bead displacement was calculated using PIVlab (Thielicke & Stamhuis, 2014). The settings are: 1) Fast-Fourier Transform (FFT), 2) a Gause 2-by-3 point sub-pixel estimator, 3) linear window interpolator and 4) three-passes (64x64, 32x32, 16x16 pixel size interrogation window equivalent to 12x12, 6x6, 3x3 μm2 with 50% overlap,). Bead displacements were converted into traction force (in Pa) by Fourier Transform method using FTTC ImageJ plugin developed by Martiel et al. (2015). The subsequent analysis was done on customed-written Matlab scripts.

Laser ablation

The laser ablation system composed of a UV-laser (355 nm, 300 ps pulse duration, 1 kHz repetition rate, PowerChip PNV-0150-100, team photonics) was integrated into a Nikon A1R MP confocal microscope, with customized optical path and dichroic filter coaligned with the optical axis of the microscope. Position of the laser can be controlled by a mirror mounted on two linear actuators (TRA12CC, Newport), and the exposure time of the laser was controlled by a mechanical shutter (VS25S2ZM0, Uniblitz) using built-in ImageJ plugins from a PC. The system was mounted on the spinning disk confocal system described above equipped with 60X oil-immersed/1.4 NA objective. The integrated laser ablation system allows us to perform laser ablation during imaging.

Laser ablation was performed on cells expressing fluorescent-labeled myosin regulatory light chain (MRLC) to visualize actin cables Apoptosis was induced as previously described and actin cable formation monitored by imaging at time interval of 10 minutes. Once the cables

589 were visualized, a time-lapse image series was launched on the region of interest (256 x 256
590 pixels) at time interval of 1-2 seconds. A UV-laser pulse of 5nW, 5s was performed on the
591 desired myosin-rich region. Images were then taken for 5 minutes. The recoil distance of the
592 actin cable d(t) was determined by tracking the displacement of the two ends connecting to
593 cell-cell junctions. The cable could be modeled as a Kelvin-Voigt fiber (Fernandez-Gonzalez

594 et al., 2009) by fitting into equation: $d(t) - d(0) = \frac{F_0}{E} \times (1 - e^{-[(\frac{E}{\mu}) \times t]})$

595 d(t) as the recoil distance at time t

596 d(0) as the original distance between two CCJ.

597 F0 is the tensile force at the junction before ablation

598 E is the junction's elasticity

599 μ is the viscosity coefficient related to the viscous drag of the cell cytoplasm

600 The initial recoil, as such, could be derived into equation: $initial\ recoil = \frac{F_0}{\mu}$

601 By fitting each ablation event into the equation, we could derive the initial recoil value, which
602 is proportional to the tension exerted at the junction by actin cable.

603 **Image Analysis**

604 In order to obtain statistics, image acquisition settings of the same type of experiments were
605 kept constant. Images were background subtracted and contrast enhanced for visualization.
606 Intensity measurements were performed on raw images. Fluorescence intensities at the
607 extruding cell-neighboring cell edges were measured using line scan tool in ImageJ. Bleach
608 correction for confocal time-lapse imaging was performed using ImageJ EMBL Bleach
609 Correction plugin. Afterwards, we took the summation image for stack of 6 slices (z-step = 0.5
610 μm, from 1 μm to 3.5 μm above the basal plane). Intensity profiles of actin or myosin at cell-
611 cell junctions were obtained by performing a 10-pixel line scan spanning along the junction
612 and corrected by deducting the average fluorescence intensity of cell contributing to the
613 junction of interest. Average intensity and standard deviation values were obtained from this
614 final line profile. Inhomogeneity of the actin/myosin intensity was defined as Inhomogeneity
615 = Mean Intensity/90th percentile Intensity of the line profile, or as standard deviation
616 normalized by the mean intensity. To correlate the formation of actin cables with the stage of
617 extrusion, we used caspase-3 indicator DEVD-FMK conjugated to Sulfo-rhodamine (Abcam)
618 as the surrogate marker for the extrusion stage.

619 To measure the actomyosin ring localization in 3D, we measured myosin-IIA intensity on fixed
620 cells imaged by Structured Illumination Microscopy (Nikon Eclipse Ti-E inverted microscope
621 body, CSU-W1 Yokogawa head, dichroic filters. The 3D reconstruction was performed on
622 Imaris, and the ring localization can be tracked using manual point selection tool to select the
623 myosin intensity at cell-cell interface. The coordinations of points corresponding to the
624 actomyosin rings were fitted into a plane by matlab. By calculating the angle between this plane
625 and horizontal plane, the angle that the ring forms with horizontal plane can be deduced.

626

639

Author contributions.

640
641   BL conceived the project; APL, BL designed research; APL principally conducted the
642   experiments and analyzed the data with support from BL, RMM, YT and JFR; JFR developed
643   the theoretical model; RMM, YT, CTL, JFR and BL provided guidance and input; RMM
644   developed α-cat mutants; BL and CTL supervised the project; APL, JFR and BL wrote the
645   manuscript. All authors read the manuscript and commented on it.

REFERENCES

1. Ohsawa, S., J. Vaughen, and T. Igaki, *Cell Extrusion: A Stress-Responsive Force for Good or Evil in Epithelial Homeostasis.* Dev Cell, 2018. **44**(3): p. 284-296.
2. Fadul, J. and J. Rosenblatt, *The forces and fates of extruding cells.* Curr Opin Cell Biol, 2018. **54**: p. 66-71.
3. Gagliardi, P.A., et al., *MRCKalpha is activated by caspase cleavage to assemble an apical actin ring for epithelial cell extrusion.* J Cell Biol, 2018. **217**(1): p. 231-249.
4. Kuipers, D., et al., *Epithelial repair is a two-stage process driven first by dying cells and then by their neighbours.* J Cell Sci, 2014. **127**(Pt 6): p. 1229-41.
5. Rosenblatt, J., M.C. Raff, and L.P. Cramer, *An epithelial cell destined for apoptosis signals its neighbors to extrude it by an actin- and myosin-dependent mechanism.* Curr Biol, 2001. **11**(23): p. 1847-57.
6. Teng, X., et al., *Remodeling of adhesion and modulation of mechanical tensile forces during apoptosis in Drosophila epithelium.* Development, 2017. **144**(1): p. 95-105.
7. Andrade, D. and J. Rosenblatt, *Apoptotic regulation of epithelial cellular extrusion.* Apoptosis, 2011. **16**(5): p. 491-501.
8. Schwayer, C., et al., *Actin Rings of Power.* Dev Cell, 2016. **37**(6): p. 493-506.
9. Tamada, M., et al., *Two distinct modes of myosin assembly and dynamics during epithelial wound closure.* J Cell Biol, 2007. **176**(1): p. 27-33.
10. Abreu-Blanco, M.T., J.M. Verboon, and S.M. Parkhurst, *Coordination of Rho family GTPase activities to orchestrate cytoskeleton responses during cell wound repair.* Curr Biol, 2014. **24**(2): p. 144-55.
11. Wu, S.K., et al., *Cortical F-actin stabilization generates apical–lateral patterns of junctional contractility that integrate cells into epithelia.* Nature Cell Biology, 2014. **16**(2): p. 167-178.
12. Lubkov, V. and D. Bar-Sagi, *E-cadherin-mediated cell coupling is required for apoptotic cell extrusion.* Curr Biol, 2014. **24**(8): p. 868-74.
13. Grieve, A.G. and C. Rabouille, *Extracellular cleavage of E-cadherin promotes epithelial cell extrusion.* J Cell Sci, 2014. **127**(Pt 15): p. 3331-46.
14. Michael, M., et al., *Coronin 1B Reorganizes the Architecture of F-Actin Networks for Contractility at Steady-State and Apoptotic Adherens Junctions.* Dev Cell, 2016. **37**(1): p. 58-71.
15. Kocgozlu, L., et al., *Epithelial Cell Packing Induces Distinct Modes of Cell Extrusions.* Curr Biol, 2016. **26**(21): p. 2942-2950.
16. Brugués, A., et al., *Forces driving epithelial wound healing.* Nature Physics, 2014. **10**: p. 683.
17. Ravasio, A., et al., *Gap geometry dictates epithelial closure efficiency.* Nat Commun, 2015. **6**: p. 7683.
18. Bryant, D.M., et al., *A molecular network for de novo generation of the apical surface and lumen.* Nat Cell Biol, 2010. **12**(11): p. 1035-45.
19. Jain, S., et al., *The role of single-cell mechanical behaviour and polarity in driving collective cell migration.* Nature Physics, 2020.
20. Gudipaty, S.A. and J. Rosenblatt, *Epithelial cell extrusion: Pathways and pathologies.* Semin Cell Dev Biol, 2017. **67**: p. 132-140.
21. Saitoh, S., et al., *Rab5-regulated endocytosis plays a crucial role in apical extrusion of transformed cells.* Proc Natl Acad Sci U S A, 2017. **114**(12): p. E2327-E2336.
22. Seddiki, R., et al., *Force-dependent binding of vinculin to alpha-catenin regulates cell-cell contact stability and collective cell behavior.* Mol Biol Cell, 2018. **29**(4): p. 380-388.
23. Thomas, W.A., et al., *alpha-Catenin and vinculin cooperate to promote high E-cadherin-based adhesion strength.* J Biol Chem, 2013. **288**(7): p. 4957-69.

24.   Yao, M., et al., *Force-dependent conformational switch of alpha-catenin controls vinculin binding.* Nat Commun, 2014. **5**: p. 4525.

25.   Chen, T., et al., *Large-scale curvature sensing by directional actin flow drives cellular migration mode switching.* Nature Physics, 2019. **15**(4): p. 393-402.

26.   Poujade, M., et al., *Collective migration of an epithelial monolayer in response to a model wound.* Proc Natl Acad Sci U S A, 2007. **104**(41): p. 15988-93.

27.   Cochet-Escartin, O., et al., *Border forces and friction control epithelial closure dynamics.* Biophys J, 2014. **106**(1): p. 65-73.

28.   Nier, V., et al., *Tissue fusion over nonadhering surfaces.* Proc Natl Acad Sci U S A, 2015. **112**(31): p. 9546-51.

29.   Slattum, G., et al., *Autophagy in oncogenic K-Ras promotes basal extrusion of epithelial cells by degrading S1P.* Curr Biol, 2014. **24**(1): p. 19-28.

30.   Vedula, S.R., et al., *Mechanics of epithelial closure over non-adherent environments.* Nat Commun, 2015. **6**: p. 6111.

31.   du Roure, O., et al., *Force mapping in epithelial cell migration.* Proc Natl Acad Sci U S A, 2005. **102**(7): p. 2390-5.

32.   Mandato, C.A. and W.M. Bement, *Contraction and polymerization cooperate to assemble and close actomyosin rings around Xenopus oocyte wounds.* J Cell Biol, 2001. **154**(4): p. 785-97.

33.   Lee, P. and C.W. Wolgemuth, *Crawling cells can close wounds without purse strings or signaling.* PLoS Comput Biol, 2011. **7**(3): p. e1002007.

34.   Staddon, M.F., et al., *Cooperation of dual modes of cell motility promotes epithelial stress relaxation to accelerate wound healing.* PLoS Comput Biol, 2018. **14**(10): p. e1006502.

35.   Fernandez-Gonzalez, R., et al., *Myosin II dynamics are regulated by tension in intercalating cells.* Dev Cell, 2009. **17**(5): p. 736-43.

36.   Priya, R., et al., *Coronin 1B supports RhoA signaling at cell-cell junctions through Myosin II.* Cell Cycle, 2016. **15**(22): p. 3033-3041.

37.   Toyama, Y., et al., *Apoptotic force and tissue dynamics during Drosophila embryogenesis.* Science, 2008. **321**(5896): p. 1683-6.

38.   Vedula, S., et al., *Microfabricated Environments to Study Collective Cell Behaviors*, in *Micropatterning in Cell Biology, Part B*, M. Piel and M. Thery, Editors. 2014.

Fig.1
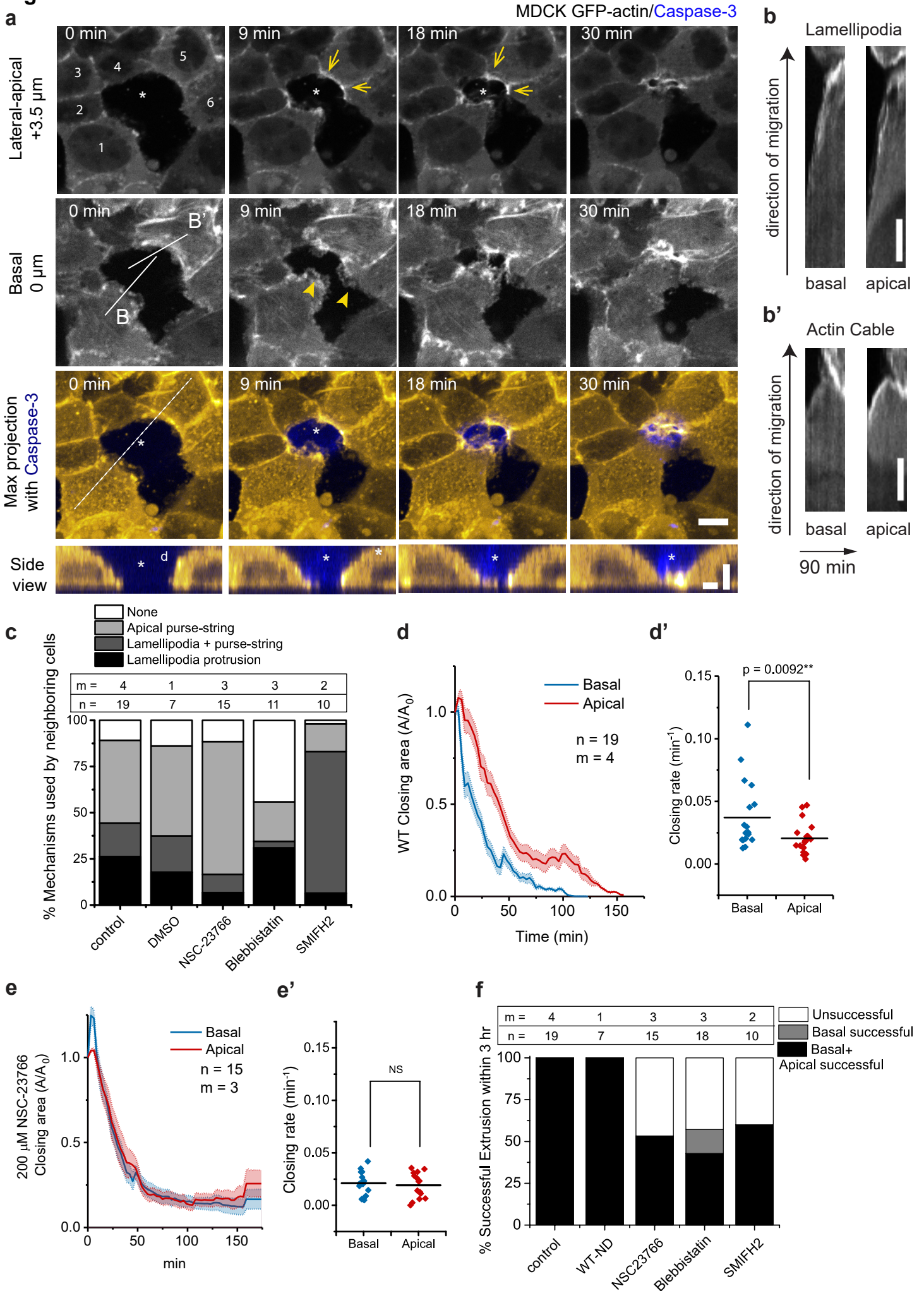
Fig. 1: Epithelial extrusion depends on dual-mechanism mode: basal lamellipodia protrusion and purse-string formation.

(a) Confocal time-lapse evolution of a non-fluorescent WT MDCK cell (asterisk) extruding from mosaic monolayer with MDCK GFP-sctin cells as neighbors. Arrows indicate actin cable formation, and arrowheads indicate lamellipodia protrusions. Colored panels represent maximum intensity projections from basal plane to +9 µm apical plane. Scale bar = 10 µm. Bottom panel: side view along dashed line showing wedged-shape when lamellipodia protrusion and non-uniform actomyosin cables take places during extrusion. Vertical scale bar = 5 µm. Horizontal scale bar = 10 µm.

(b – b') Kymographs performed along the connected line for lamellipodia (labeled as B in panel a) and along the connected line for actin cable (labeled as B' in panel a), at basal and apical planes. Vertical scale bar = 5µm. Time duration for all kymographs was 90 min.

(c) Proportion of the mechanism chosen by neighboring cells in control conditions versus different pharmacological perturbation conditions: 200 µM NSC-23766 (Rac inhibitor) and 50 µM (S)-nitro Blebbistatin (SBB, Myosin activity inhibitor) and 50 µM SMIFH2 (Formin inhibitor). 0.1% DMSO was used as additional control for drug vehicle. n indicates number of extrusion events observed. m indicates number of independent experiments (experiments carried on different days). Source data are provided as a Source Data file.

(d & e) Average relative area closure of basal and apical planes (defined as + 4 µm from the basal plane) as a function of time. The areas were normalized to area at t = 0 min. Shaded area : SEM. Number of extrusion events n = 15, and number of independent experiments m = 3. Source data are provided as a Source Data file.

(d' & e') Closing rate derived by extracting the tangent of initial phase of the area closing curve. Middle lines: mean. Paired t-tests (2-tailed) were performed as comparison for closing speed between apical versus basal plane. Number of extrusion events and number of independent experiments are same as (c). Source data are provided as a Source Data file.

(f) Successful extrusion percentage for all conditions. Basal successful indicates complete basal closure but the cells were not extruded and new junctions between neighboring cells were not formed. Successful extrusion is indicated by basal successful + apical successful. Source data are provided as a Source Data file.

Fig.2
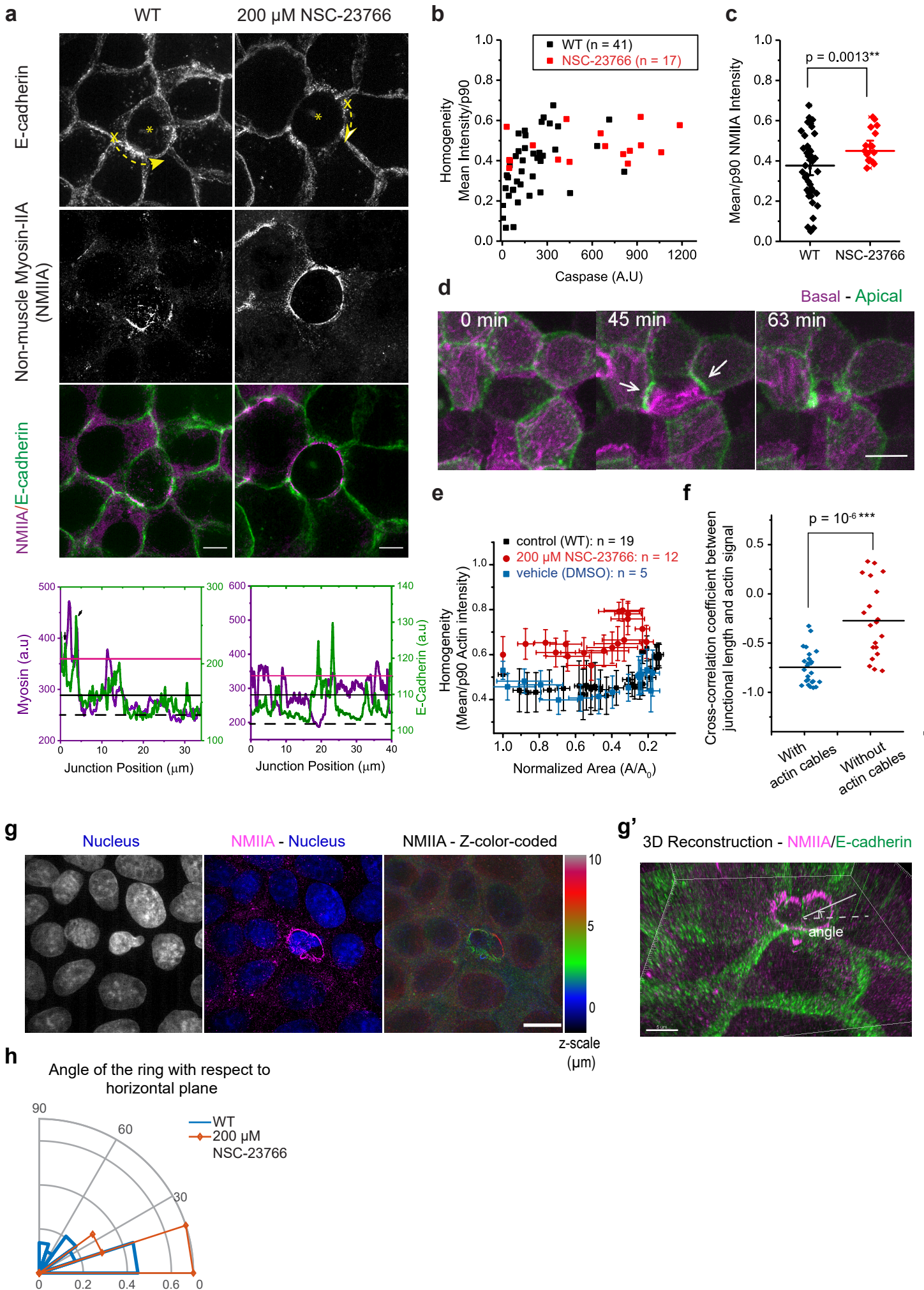
Fig. 2: Inhomogeneous actomyosin cables were observed and persistent during extrusion.

(a) Immunostaining of non-muscle myosin IIA (NMIIA) on extrusion of MDCK with GFP-E-cadherin stably expressed monolayer in WT *versus* Rac-inhibited monolayer. Images show maximal projection of z-stack from 2-6 μm above basal plane of SIM confocal image of fixed monolayer with extruding cell (asterisk). Scale bar = 10 μm. Bottom panel: line scan of 10 pixels width showing intensity profile along the junction between neighboring cells-extruding cell. X in the first panel indicates the position 0 of the line scan and the dashed arrows indicate the direction the line scan was performed. Inhomogeneous actomyosin cables were observed in WT condition but not in Rac-inhibited condition. Source data are provided as a Source Data file.

(b) Relationship between non-muscle myosin IIA intensity inhomogeneity and caspase indicator fluorescence. (Number of extrusion events: n = 41 for WT and n = 17 for Rac-inhibitor treatment. Number of independent experiments: m = 4 for WT and m = 2 for Rac-inhibitor treatment). Values closer to 1 indicate more homogeneous cables and closer to 0 indicates more non-uniform cables. Source data are provided as a Source Data file.

(c) Comparison for the inhomogeneity of actomyosin cables between WT versus Rac-inhibited monolayers by mean/p90 (normalized against the background myosin intensity). Middle lines: mean. Error bars: SEM. 2-tailed unpaired t-test was performed, and p values shown. Source data are provided as a Source Data file.

(d) Confocal time-lapse evolution of MDCK cell stably expressing Lifeact Ruby for actin undergoing extrusion. Basal plane (magenta) is superimposed with apical plane (green, 3.5 μm above the basal plane). Scale bar = 10 μm. T = 0 is defined as the time point right after laser induction.

(e) Average inhomogeneity of actin cable (indicated by actin signals in live imaging) as a function of area normalized against value at time 0. Values close to 1 indicate more inhomogeneous actin cables and values close to 0 indicate more inhomogeneous actin cables. Error bars: SEM. Number of independent experiments: WT: m = 3; Rac-inhibitor (NSC-23766): m = 2; DMSO (drug control): m = 1. Source data are provided as a Source Data file.

(f) Cross-correlation analysis between junctional length and average junctional intensity on individual junctions. (n = 26 for edges with cables and n = 20 for edges without cables in 7 extrusions, 3 independent experiments). Middle lines: mean. Two-tailed unpaired t-test was performed. See more on Supplementary Fig. 5b. Source data are provided as a Source Data file.
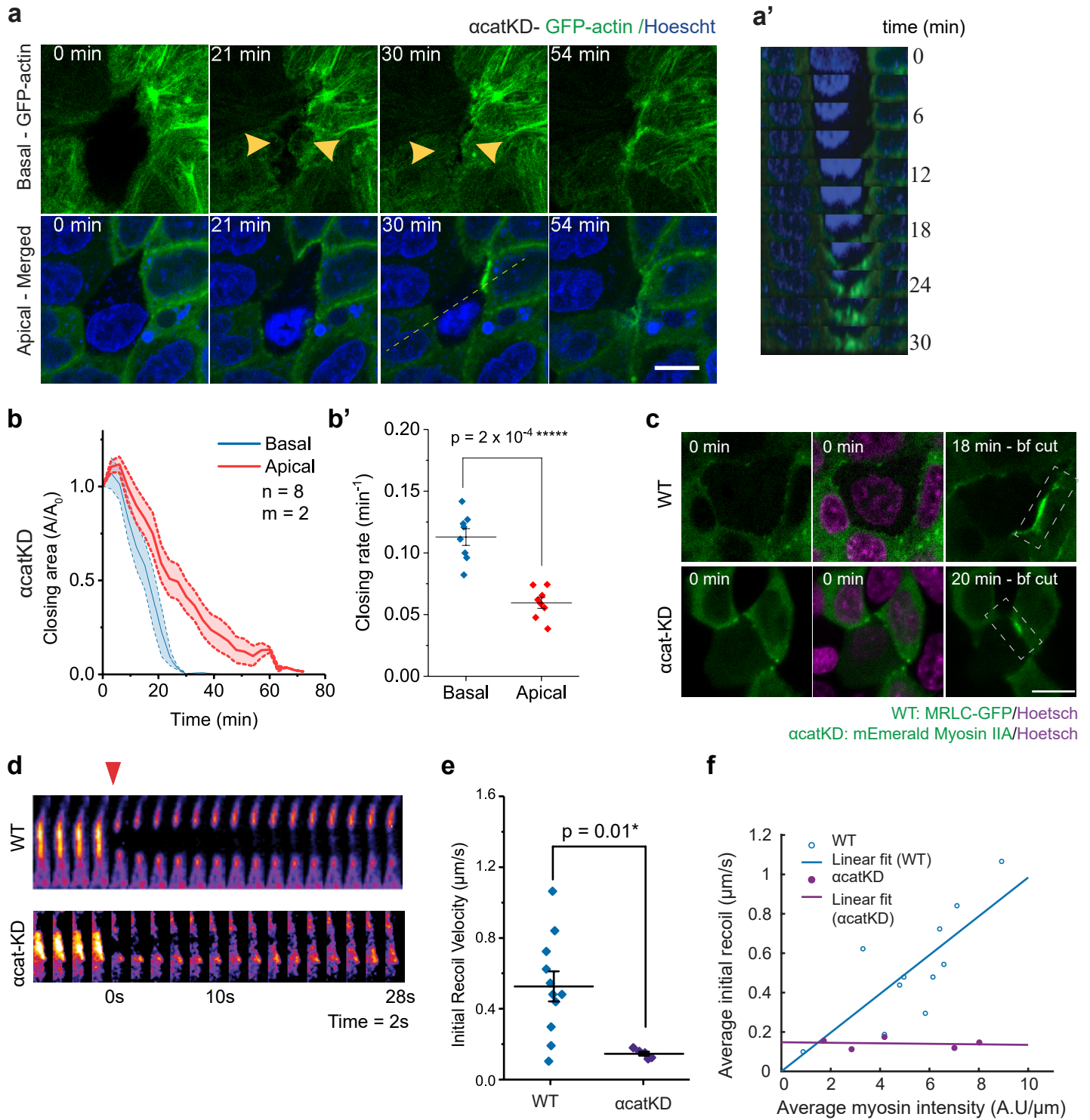
(g & g') Localization of actomyosin cables in 3D shown by z-color coded and 3D reconstruction for immunostaining of myosin IIA in WT cells.

(g) Immunostaining of MDCK cells extruding from monolayer (extruding cell at the center). i) DAPI channel. ii) Merged of DAPI and AlexaFluor-568 channel. iii) Myosin staining color-coded according to the height of the monolayer. The contrasting localization of myosin around nucleus at two separated planes (~3 μm *versus* 7 μm at each side) suggested the partitioning of the purse-string into two rings which are tilted.

(g') 3D reconstruction for images in (g). A circular fit was performed on each ring on 3D reconstruction images. The angle at which the circle formed with horizontal plane xy was defined as shown on the image.

(h) Histogram of distribution of angles that the purse-string ring forms w.r.t horizontal plane. (WT: n = 32 rings in m = 19 extrusion events; NSC-23766 (Rac-inhibitor): n = 10 rings in m = 11 extrusion events). Source data are provided as a Source Data file.

Fig.3

a αcatKD- GFP-actin /Hoescht

a' time (min)

b αcatKD

b' p = 2 x 10^{-4} *****

c WT: MRLC-GFP/Hoetsch
αcatKD: mEmerald Myosin IIA/Hoetsch

d Time = 2s

e p = 0.01*

f

Fig. 3: Reduction of cell-cell junction (CCJ) strength impairs contractile purse-string formation and renders extrusion depend on lamellipodia protrusion.

(a-a') Time-lapse imaging of αcat- knocked-down MDCK cells (α-catKD-GFP-actin) expressing GFP-actin. The cell in the middle undergoes extrusion. (a) Top panels: basal plane, bottom panels: apical plane (+ 4 μm above basal plane). Scale bar = 10 μm. (a') Side view along the yellow-dashed line, reconstructed from a Z-stack of 7 μm (stacks spaced of 0.5 μm).

(b) Average relative area closure of basal versus apical planes (defined as + 4 μm from the basal plane) for α-catKD-GFP-actin MDCK cells. The areas were normalized to area at t = 0min. Shaded area: SEM. n = 8 indicates number of extrusion from m = 2 independent experiments. Source data are provided as a Source Data file.

(b') Closing rate derived by extracting the tangent of initial phase of the area closing curve. Middle lines: mean. Error bars: SEM. Paired t-tests (2-tailed) were performed. Source data are provided as a Source Data file.

(c-f) Laser ablation at cell-cell junction (area denoted by dashed rectangle) during extrusion on WT MDCK cells expressing GFP-MRLC and αcatKD MDCK cells expressing m-Emerald Myosin IIA. N = 11 for WT and N = 5 for αcatKD indicate number of laser ablation experiments. Source data are provided as a Source Data file.

(c) Top view images of myosin accumulation at cell-cell junctions. t = 0 min refers to the initiation of laser-induced extrusion. Images in the last panel (bf cut = before cut) are at the time point the cable becomes visible and at when laser ablation was performed on the cable. Dashed rectangles indicate the junction on which laser ablation was performed.

(d) Evolution of myosin signal from the rectangular area in (c) before and after laser ablation of cell-cell junctions. Enhanced myosin recruitment is shown in FIRE LUT. Arrowhead indicated the point at which laser ablation is performed.

(e) Comparison between the initial recoil velocity – which reflect junction tension - after ablation for WT versus αcatKD. Middle lines: mean. Error bars: SEM. Unpaired t-test was performed. Number of laser ablation experiments WT: n = 11 and αcatKD: n = 5.

(f) Average initial recoil velocity as a function of average myosin accumulation prior to laser ablation. Middle lines: mean. Error bars: SEM. Linear regression was performed to fit.

Fig.4

a

Apical | 0 min | 9 min | 39 min | 72 min

Basal | 0 min | 9 min | 39 min | 72 min

WT - LifeActRuby   αcatKD - GFP-actin

b

p = 0.015*

Speed of leading edge towards extrusion center (µm/min)

WT   αcatKD

c

□ None
▨ Lamellipodia + purse-string
▨ Apical purse-string
■ Lamellipodia

m = 4   2   5   2   2
n = 19 11 17 15 12

WT, αcat-KD, αcat-L344P, αcat-WTres, αcat-ΔMod

d

Relative basal area (A/A$_0$)

- - - αcatKD
—— αcat-L344P
—— αcat-WTres
- - - αcat- ΔMod

Time (min)

e

Basal Closing Time (min)

*
**
***
*

WT, αcatKD, αcat-L344P, αcat-WTres, αcat-ΔMod

f

Extrusion Completion Time (min)

* ns ns ns
* *   *   ns
   ns ns ns
       ns

WT, αcatKD, αcat-L344P, αcat-WTres, αcat-ΔMod

Fig.4: Tuning cell-cell junction strength by α-catenin could adjust the preferential mode of extrusion but not extrusion efficiency.

(a – b) Laser-induced extrusion in mixed WT and αcatKD MDCK co-culture. The extruding cells are WT (a) Top view of an example of extrusion from the mosaic monolayer. Scale bar = 10 μm. (b) Velocity towards the center of extrusion at basal side for each type of neighbor. Middle lines: mean. Error bars: SEM. N = 20 extrusion events. 2-tailed, unpaired t-test was performed.

(c) The contribution of mechanism at individual neighbors in single cell type cultures of different α-catenin mutant cells. αcat-KD: MDCK cells with stable α-catenin knock-down. αcat-L344P: MDCK α-catenin knock-down cells rescued with α-catenin-L344P mutant. αcat-WTres: MDCK α-catenin knock-down cells rescued with wild-type GFP-α-catenin. αcat-ΔMod: MDCK α-catenin knock-down cells rescued with α-catenin-ΔMod mutant. n: number of extrusion events. m: number of independent experiments.

(d-f) (d) Evolution with time of relative closure area changes at basal plane for cells expressing the different α-catenin mutants. Number of extrusion events and number of independent experiments are same in (c). (e): Mean basal closing times. (f) Mean extrusion completion time (both apical and basal area are closed). Middle lines: mean. Error bars: SEM. 1-way ANOVA ($p < 0.01**$) followed by pair-wise comparison with Benjamini, Krieger and Yekutieli correction for false discovery rate was performed. Significant level: ns: non-significant; $p < 0.05*$; $p < 0.01**$; $p < 0.001***$, $p < 0.0001****$. Source data are provided as a Source Data file.

Fig.5
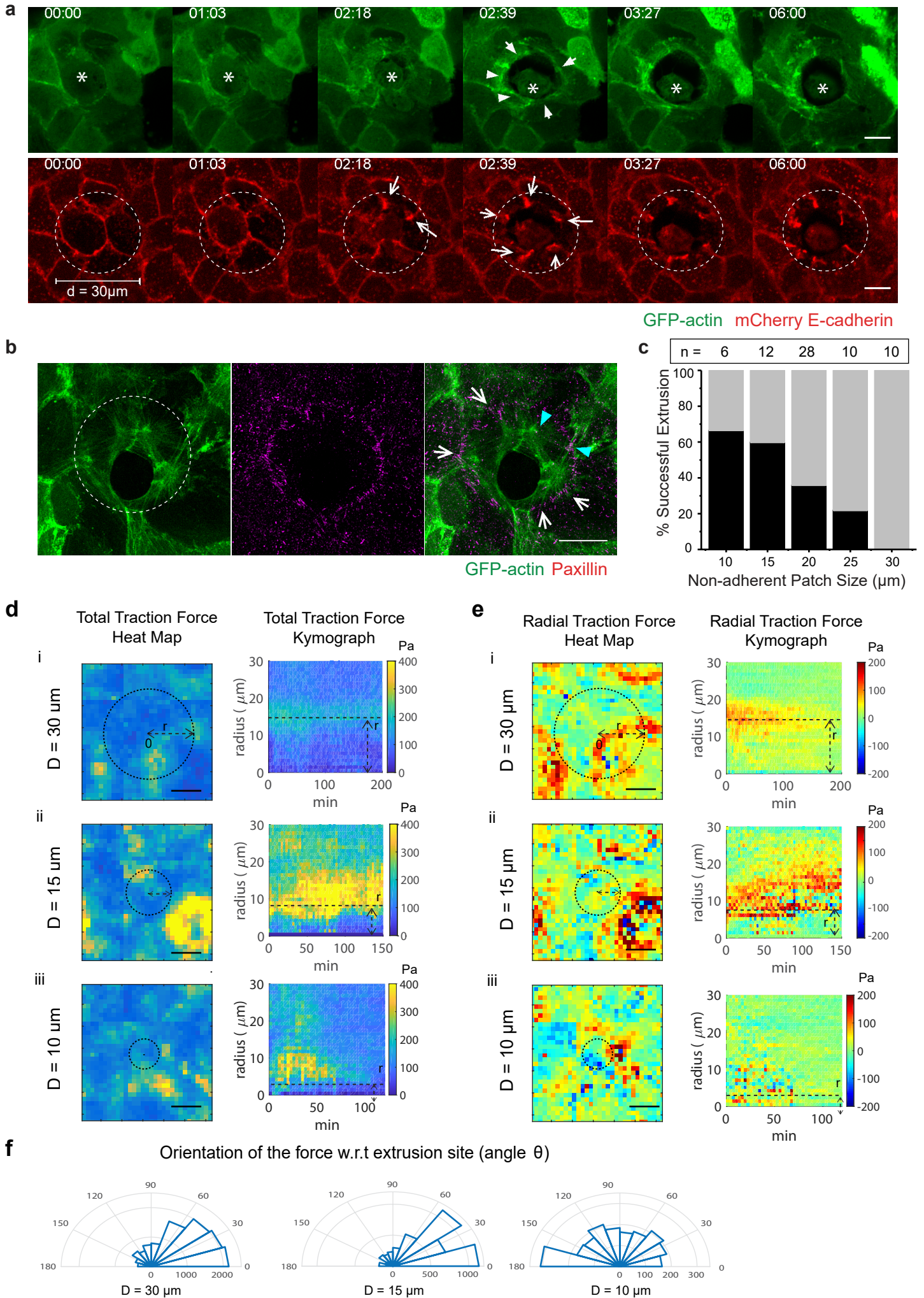
Fig. 5: Substrate adherence influences the uniformity of actomyosin cables, extrusion efficiency and forces contribution by purse-string/lamellipodia.

(a) Confocal time-lapse imaging of laser-induced extrusion of a mCherry-E-cadherin, GFP-actin expressing MDCK cells sitting on 30 μm nonadherent patch. The dying cell (marked with an asterisk) is not successfully extruded. Whites arrows, dashed circles. Scale bar = 10 μm.

(b) Structural Illuminated Microscopy (SIM) images of a fixed extruding GFP-actin expressing MDCK cell on non-adhesive patch. Cells were fixed and stained with anti-Paxillin antibodies. White arrow shows the radial actin cable connected with focal adhesion. Cyan arrowheads show cables anchoring between cell-cell junctions (indicated by actin converging points) and focal adhesion (indicated by paxillin staining). Scale bar = 10 μm.

(c) Quantification of the percentage of successful extrusion in function on non-adhesive patch size i. n indicates the number of extrusion events. Source data are provided as a Source Data file.

(d & e) Traction force measurement on non-adherent patches. Source data are provided as a Source Data file.

(d) Heat map (left) and kymograph of average total traction magnitude (right) with respected to the center of the non-adhesive patches as a function of time. Color bar indicated the force magnitude (in Pa). Heat map was the average over 3 hours for 5 different extrusions, and kymograph was the average of 5 different extrusions.

(e) Heat map (left) and kymograph of average radial traction force (right) with respected to the center of the non-adhesive patches as a function of time. Color bar indicated the force magnitude (in Pa). +1 indicates forces pointing towards center (inwards) and -1 indicates forces pointing away from center (outwards). Color bar indicated the force magnitude (in Pa). The kymograph was the average of 4-6 different extrusions.

(f) Polar histogram showing the orientation of the force with respected to extrusion site on 10 μm, 15 μm and 30 μm non-adhesive patch. Angle θ is the radial angle of the force vector w.r.t the center of non-adhesive patch. θ < 90 shows inwards pointing forces and 90 < θ < 180 shows outwards pointing forces.

Fig.6
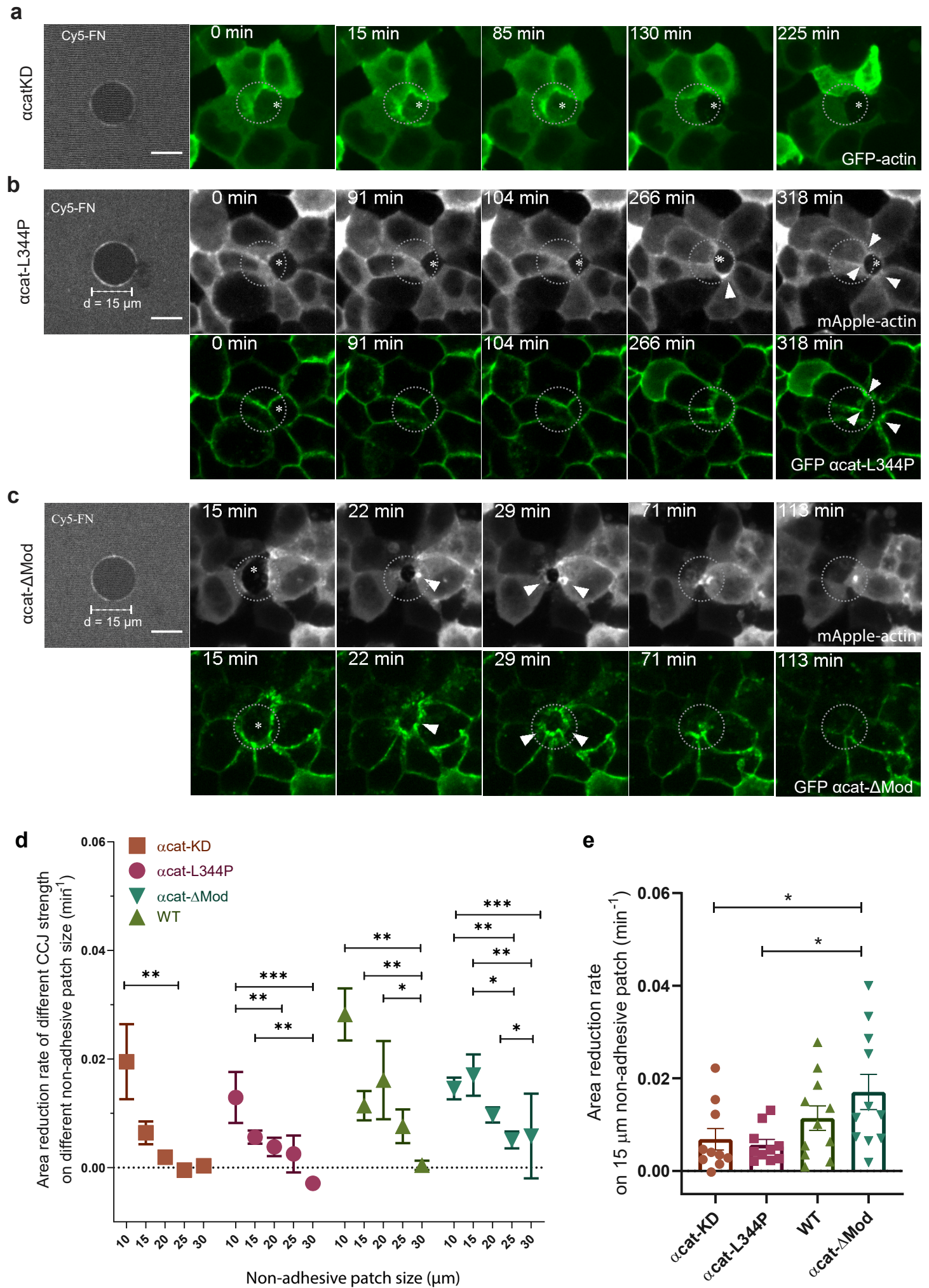
Fig. 6: Interplay of cell-substrate adhesion and cell-cell junction strength on regulating dual-mechanism modes of extrusion

(a-c) Representative examples of extrusion of cells with different CCJ strength on 15 μm non-adhesive patches. The first image shows the substrate coated with Cy-5 Fibronectin with darker field represents non-adhesive area. 2nd to 5th panel: confocal live imaging of (a) αcatKD cells (b) αcat-L344P cells and (c) αcat- ΔMod cells. Arrowheads indicated the accumulation of αcat at tricellular points corresponding to cable formation. Scale bar = 10 μm.

(d) Quantification of the mean area reduction rate of cell extrusion for the four types of cells on varying non-adhesive patch sizes. Error bars indicated SEM. Non-parametric Kruskal-Wallis test was performed for each group, followed by pair-wise comparisons. Significant level: $p < 0.05$*; $p < 0.01$**; $p < 0.001$***. N = 10-28 for each condition. Source data are provided as a Source Data file.

(e) Quantification of the rate of area closing for the same four types of cells on 15 μm non-adhesive patches. Number of extrusion events: WT: N = 10; αcat-KD: N = 10; αcat-L344P: 3: N = 10; αcat-ΔMod: N = 11. At least 2 independent experiments were performed for each condition Non-parametric Kruskal-Wallis test ($p < 0.01$**) followed by pair-wise comparison was performed. Significant level: $p < 0.05$*; $p < 0.01$**. Source data are provided as a Source Data file.

Fig.7
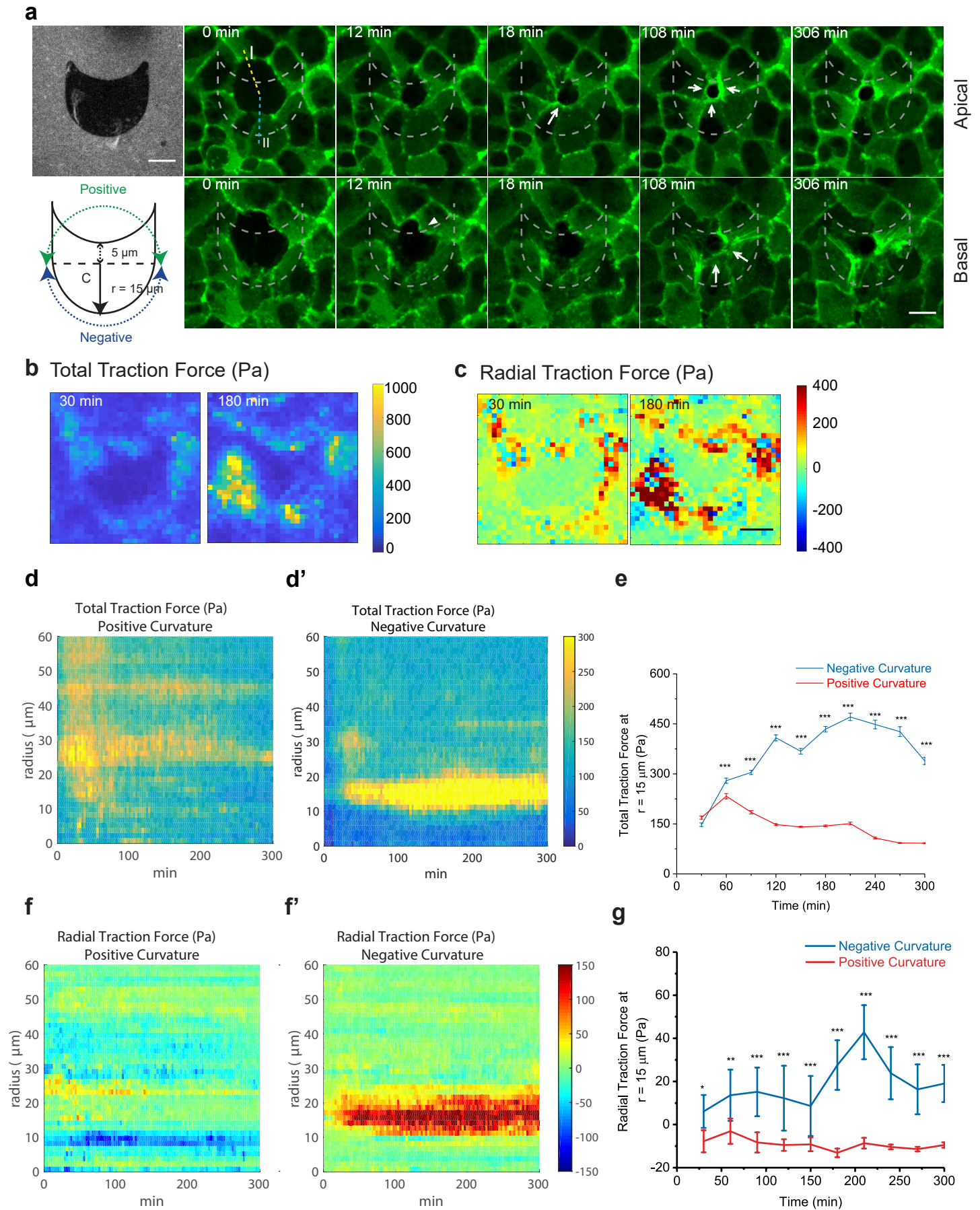
Fig. 7: Anisotropic non-adhesive shape dictated preferential mode of extrusion.

(a) Confocal time-lapse images of cell extrusion on non-isotropic non-adhesive shapes. First panel, first image: substrate coated with Cy5 fibronectin showing non-adherent patches (darker phase). Second panel, first image: schematic of the anisotropic patch design. 2nd-5th images: time-lapse confocal imaging at apical plane (top panel) and basal plane (bottom panel) of GFP-actin expressing monolayer centered on a cell extruding above a nonadherent patch (non-fluorescent cell). The negatively-curved region induced the earlier formation of contractile actin cables (white filled arrow). Scale bar = 10 μm.

(b-c) Average heat map for total (b) and radial traction forces in Pascal (Pa) (c) averaged over 4 extrusion events (One event each experiment). The force magnitude was color-coded on the color scale bar (in Pa). Scale bar = 10 μm. Source data are provided as a Source Data file.

(d-d') Kymographs for total traction forces around extrusion sites for positively-curved (P) regions and negatively-curved (N) regions. The force magnitude was color-coded on the color scale bar (in Pa). m = 4 extrusion events. Source data provided as a Source Data file.

(e) Averaged traction force magnitude at r = 15 μm (equivalent to the distance between center to negative edges) in function of time. n = 20 averaged force vectors for each time point, averaged from m = 4 extrusion events. Error bars indicate SEM. 2-tailed unpaired t-test was used for comparing between negative curvature and positive curvature. $p < 0.001$***. Source data are provided as a Source Data file.

(f-f'). Kymographs for radial traction forces around extrusion sites for positively-curved (P) regions and negatively-curved (N) regions. The force magnitude was color-coded on the color scale bar (in Pa). n = 20 averaged force vectors for each time point, averaged from m = 4 experiments. Source data are provided as a Source Data file.

(g) Averaged radial traction force at r = 15 μm in function of time. Replicates number same as (e). Error bars indicate SEM. 2-tailed unpaired t-test was used for comparison between negative curvature and positive curvature. $P < 0.001$***. Source data are provided as a Source Data file.

Fig.8
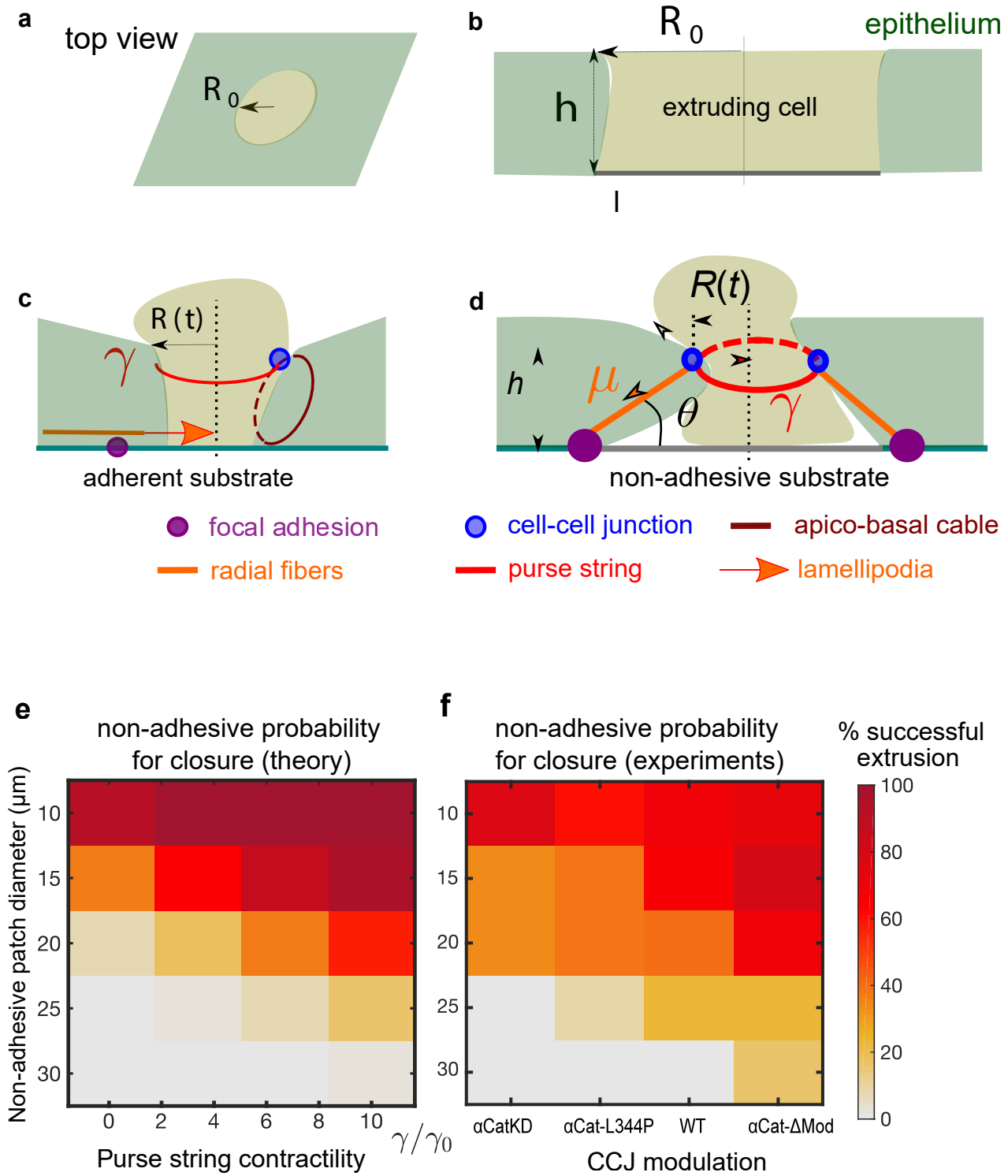
Fig.8: Integrative model for extrusion

(a-d) Sketch of the model.

(a) Side view with the extruding cell (represented as a light green disk) and the surrounding epithelium.

(b) Side view at the initial stage of extrusion with the laser ablated patch (corresponding to one or several cells) of a radius R0.

(c) Adherent case: a combination of lamellipodia, apico-basal cable, and non-uniform purse-string contribute to the extrusion process.

(d) Non-adhesive case: a multi-cellular purse-string of tension γ (red circle) contributes to the extrusion dynamics while apico-basal cables (orange line), with a tension denoted μ, provide a resistive contribution. Arrows represent the forces acting on a cell-cell junction (represented by a blue circle).

(e) Phase diagram of the predicted percentage of successful extrusions in terms of the non-adhesive patch diameter (2 R_0) and of the purse string contractility.

(f) Phase diagram of the experimentally measured percentage of successful extrusions in terms of the non-adhesive patch diameter and of the CCJ perturbation. Number of extrusion events: N = 10-28 for each condition.